communications physics

Article

https://doi.org/10.1038/s42005-024-01751-1

Morphometry on the sphere: Cartesian and irreducible Minkowski tensors explained and implemented

Caroline Collischon [1] ✉, Michael A. Klatt[2,3,4], Anthony J. Banday[5], Manami Sasaki [1] & Christoph Räth [2,4]

Minkowski tensors are comprehensive shape descriptors that robustly capture *n*-point information in complex random geometries and that have already been extensively applied in the Euclidean plane. Here, we devise a framework for Minkowski tensors on the sphere. We first advance the theory by introducing irreducible Minkowski tensors, which avoid the redundancies of previous representations. We, moreover, generalize Minkowski sky maps to the sphere. These maps are a concept of local anisotropy, which easily adjusts to masked data. We demonstrate the power of our new procedure by applying it to simulations and real data of the Cosmic Microwave Background, finding an anomalous region close to the well-known Cold Spot. The accompanying open-source software, `litchi`, used to generate these maps from data in the HEALPix-format is made publicly available to facilitate broader integration of Minkowski maps in other fields, such as fluid demixing, porous structures, or geosciences more generally.

Minkowski functionals (MF) and Minkowski tensors (MT) from integral geometry[1,2] are powerful and versatile shape descriptors for random spatial structures in real space. They provide a localized and comprehensive shape analysis by characterizing, among others, symmetries and preferred directions. They provide robust access to information from *n*-point correlation functions (since they can be expressed as a sum over all *n*-point correlation functions)[3]. Yet, their calculation is much simpler than that of higher-order correlation functions, which allows for an exploitation of higher-order correlations in spatial structures that is practically inaccessible when relying on estimates of correlation functions. Furthermore, they contain information not visible to other common morphological tools, such as wavelets[4] or the mean intercept length[5].

MT have been used in a broad range of fields, such as analysis of trabecular bone structure[6], classifying the shapes of galaxies[7], fluid demixing[8], analyzing cellular, granular, and porous structures[9], source detection in gamma-ray astronomy[10,11], analyzing nuclear pasta matter[12] or applications in crystallography (e.g., Böbel et al.[13] and references therein). However, most applications have so far focused on the Euclidean space.

A prominent exception is cosmology, specifically the analysis of simulated[14,15] and reconstructed maps[16] of the Cosmic Microwave Background (CMB). The scalar MF have already been intensively used to analyze the CMB, either using single MF[17,18] or in systematic studies of all MF[19–21]. They have been used to search for non-Gaussianity in temperature and polarization, both by the Planck collaboration[22] and other groups[23–26]. Rank 2 MT on the CMB have first been used by Chingangbam et al.[27], finding consistency with Gaussianity via their approach. Following them, Joby et al.[28] found consistency with statistical isotropy and Appleby et al.[29] show the usage of rank 2 MT on redshift-space distorted Gaussian random fields in general.

In cosmology, MF and MT offer several advantages over other methods, such as two- or three-point correlation functions. Their definition in real space offers a more comprehensive, "human-readable" way to analyze all-sky data as compared to harmonic decomposition. Since they can be calculated locally for either single shapes or selected regions, MF/MT are excellent tools to search for anisotropy and provide natural ways to deal with incomplete (e.g., masked) data. Additionally, they contain higher-order information that would not be included in a 2- or 3-point correlation analysis.

Here, we introduce a pixel-based approach of calculating MF/MT of arbitrary rank on the sphere and implement it in the publicly available code `litchi`[30]. Unlike the aforementioned references where the MF/MT were calculated globally, we devise a localized analysis, dubbed Minkowski Maps

[1]Dr. Karl-Remeis Sternwarte, Erlangen Centre for Astroparticle Physics, Friedrich-Alexander Universität Erlangen-Nürnberg, Bamberg, Germany. [2]Deutsches Zentrum für Luft- und Raumfahrt (DLR), Institut für KI Sicherheit, Ulm, Germany. [3]Deutsches Zentrum für Luft- und Raumfahrt (DLR), Institut für Materialphysik im Weltraum, Köln, Germany. [4]Department of Physics, Ludwig-Maximilians-Universität München, Munich, Germany. [5]IRAP, Université de Toulouse, CNRS, CNES, UPS, Toulouse, France. ✉e-mail: caroline.collischon@fau.de

(MM). We start by defining the classical Cartesian MF/MT on the sphere and show how to use scalars to represent their information about the degree of anisotropy for rank 2 and 4. Next, we define, to the best of our knowledge for the first time, irreducible MT on the sphere, providing access to scalar shape information at arbitrary rank. The MM visualize local information. We provide methods to calculate these maps on the sphere and apply them to examples that compare Cartesian and irreducible MT (which can serve as a reference for users). Note that in contrast to MM in Euclidean space a MM on the sphere requires the concept of parallel transport on the sphere, as explained below. Finally, we apply our methods to Planck CMB temperature data and simulations. Importantly, our methods provide additional information compared to the more common tools as they do not strongly react to absolute values of a random field but rather to its shape and symmetries. Thus, we find two noteworthy spots, one in the southern Galactic hemisphere close (but not statistically related) to the Cold Spot[31], and the other above the Galactic plane.

Results

The main result of this work consists in bringing the MT to the surface of the sphere. To this end, we first state the current methods for Euclidean space and then adapt them to the sphere.

Theory of MT: Euclidean plane vs sphere

In the Euclidean plane, the three MF are given by area, perimeter, and Euler characteristic. In general the MF of a compact body K with a smooth contour ∂K are defined as

$$W_0(K) = \int_K \mathrm{d}r,\ W_\nu(K) = \int_{\partial K} G_\nu\, \mathrm{d}r \tag{1}$$

where $\nu \in \{1, 2\}$, $G_1 = 1$ and $G_2 = \kappa$, the sectional curvature. The definition can be straightforwardly extended to more general domains, e.g., polyconvex sets[2,32]. Ensemble expectation values for the MF of Gaussian random fields are well known via the Gaussian kinematic formula[33] and more recently, advancements have been made for non-Gaussian fields[34–36].

The MF are additive ($W_\nu(A) + W_\nu(B) = W_\nu(A \cup B) - W_\nu(A \cap B)$). In fact, in Euclidean space, Hadwiger's theorem states that any additive functional of convex shapes that is continuous and motion invariant (i.e., scalar) can be expressed as a linear combination of MF[37]. In that sense, MF capture all additive shape information.

On the sphere, an analogous theorem holds as proven by Klain and Rota[ref. 38, Theorem 11.3.1]. In particular, shapes in pixel images can be expressed as unions of single (convex) pixels, making them a good target for MF/MT analysis. Grayscale images with varying brightness can be analyzed by applying a threshold, interpreting everything above the threshold as part of the body, and optionally adding up the MF/MT obtained at several thresholds.

The analysis with MF can be naturally generalized for anisotropic structures to motion covariant tensors, the so-called MT, which are defined in Euclidean space as follows. Using the symmetric tensor product with

$$\mathbf{n}^b := \underbrace{\mathbf{n} \otimes \ldots \otimes \mathbf{n}}_{b\ \text{times}} \tag{2}$$

and components

$$(\mathbf{n}^b)_{i_1 \ldots i_b} = n_{i_1} \ldots n_{i_b}. \tag{3}$$

The translation invariant Cartesian MT of rank b are then given by

$$W_\nu^{0,b}(K) := \int_{\partial K} \mathbf{n}^b G_\nu\, \mathrm{d}r \tag{4}$$

where different communities may use different (constant) prefactors. There are also translation covariant MT, which we omit here since there is no generic generalization to the sphere. Note that $W_\nu^{0,1}(K) = 0$ for closed K in flat space. Alesker proved a theorem analogous to Hadwiger for MT[39]. However, such a theorem is unknown on the sphere. Further properties of the MT (useful for applications) can, e.g., be found in other works[9,32,40].

On the sphere, $\mathbf{n}$ is interpreted as the tangent space vector perpendicular to the contour. It is normalized according to the metric of the spherical surface, $g_{00} = 1, g_{11} = \sin^2(\theta), g_{01} = g_{10} = 0$. We will subsequently use the notation n^μ for its components with $\mu \in \{0, 1\}$, $n^0 = n^\theta$; $n^1 = n^\phi$ in the usual coordinates on the sphere; see Fig. 1. Tensor integration on the sphere can be done according to Fabian (1957)[41], who presents an expansion method analogous to Taylor expansions.

Scalar representation based on Cartesian representation

To visualize and analyze the degree of anisotropy with MT, they need to be brought into a scalar form that is invariant under rotation. Several possible representations are available in the Euclidean plane that can be generalized to the sphere. Each option captures different information. The trace operator is a straightforward choice. For $W_1^{0,2}$, we obtain

$$\begin{aligned}\mathrm{tr}\left(W_1^{0,2}(K)\right) &= \int_{\partial K} (\mathbf{n} \otimes \mathbf{n})^{\mu\nu} g_{\nu\mu}\, \mathrm{d}r = \int_{\partial K} (n^0)^2 + \sin^2(\theta)\,(n^1)^2\, \mathrm{d}r \\ &= \int_{\partial K} \mathrm{d}r = W_1^{0,0}(K),\end{aligned} \tag{5}$$

where we inserted the metric tensor.

More morphological information is contained in the ratio of eigenvalues, i.e., the eigenvalue quotient (EVQ). The eigenvector equation for eigenvalue λ for a vector v^μ is given by

$$W^{\mu\nu} g_{\nu\alpha} v^\alpha = \lambda v^\mu \tag{6}$$

$$\begin{pmatrix} W^{00} & W^{01}\sin^2(\theta) \\ W^{10} & W^{11}\sin^2(\theta) \end{pmatrix} \begin{pmatrix} v^0 \\ v^1 \end{pmatrix} = \lambda \begin{pmatrix} v^0 \\ v^1 \end{pmatrix} \tag{7}$$

where $W^{\mu\nu} = (W_1^{0,2})^{\mu\nu}$ are the components of $W_1^{0,2}$.

Since $W_1^{0,2}$ is symmetric, the eigenvectors are orthogonal. For an elongated shape with 2-fold symmetry, one eigenvalue will be larger than the other so that the ratio is a useful measure for elongation. In this paper, we divide the larger eigenvalue by the smaller one. The eigenvectors themselves can be used to find the preferred orientation of the body.

An approach to rank 1 tensors was shown by Joby et al.[42], who integrated over the gradient of the field. In our framework, this tensor corresponds to $W_1^{0,1}$, where the contour is given by contours of the field at several thresholds. This tensor vanishes for closed contours in Euclidean space. When looking at a non-closed shape in a small enough region to keep spherical effects negligible, its length measures the directionality of the contours (how much the remaining gradient prefers one direction). Alternatively one can use the direction of that vector to show the total normal of the remaining contours.

Rank 4 tensors can be tackled by taking their symmetries into account. We will do this along the lines of a method shown by Mehrabadi et al.[43], where the authors considered three-dimensional rank 4 tensors as six-dimensional rank 2 tensors (that is, 6×6 matrices) using their symmetries. In this representation, eigenvalues can be easily calculated, and the corresponding eigenvectors can then be reinterpreted as eigentensors in the original space.

In our case, a symmetric two-dimensional rank 4 tensor can be represented by a 3×3 matrix whose eigenvectors are reinterpreted as rank 2 tensors. Multiplication of the rank 4 tensor with a rank 2 tensor $\sigma^{\mu\nu}$ is given in components by

$$\sigma'^{\mu\nu} = W^{\mu\nu\alpha\beta} g_{\alpha\gamma} g_{\beta\delta}\, \sigma^{\gamma\delta} \tag{8}$$

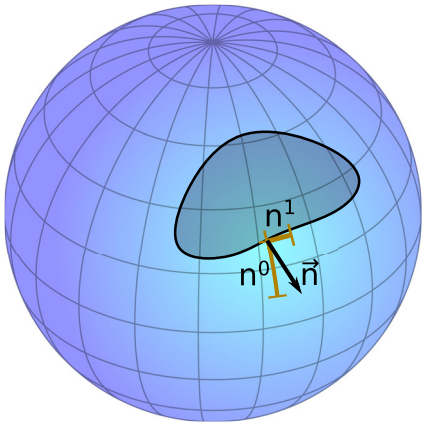

Fig. 1 | Definition of n on the sphere. It is perpendicular to the contour of the body to be analyzed (black shape) and is decomposed into its components on the spherical surface (orange bars). No embedding into the three-dimensional space takes place.

$$\sigma'^{00} = W^{0000} g_{00} g_{00} \sigma^{00} + 2W^{0001} g_{00} g_{11} \sigma^{01} + W^{0011} g_{11} g_{11} \sigma^{11} \quad (9)$$

$$\sigma'^{01} = \sigma'^{10} = W^{0100} g_{00} g_{00} \sigma^{00} + 2W^{0101} g_{00} g_{11} \sigma^{01} + W^{0111} g_{11} g_{11} \sigma^{11} \quad (10)$$

$$\sigma'^{11} = W^{1100} g_{00} g_{00} \sigma^{00} + 2W^{1101} g_{00} g_{11} \sigma^{01} + W^{1111} g_{11} g_{11} \sigma^{11} \quad (11)$$

where the factor 2 comes from the symmetry of all involved tensors. Note that W has only 5 distinct components (no change under permutation of indices). Inserting the components of g and writing in matrix form gives the equation for eigentensor σ with eigenvalue λ as

$$\begin{pmatrix} W^{0000} & 2W^{0001}\sin^2(\theta) & W^{0011}\sin^4(\theta) \\ W^{0100} & 2W^{0101}\sin^2(\theta) & W^{0111}\sin^4(\theta) \\ W^{1100} & 2W^{1101}\sin^2(\theta) & W^{1111}\sin^4(\theta) \end{pmatrix} \begin{pmatrix} \sigma^{00} \\ \sigma^{01} \\ \sigma^{11} \end{pmatrix} = \lambda \begin{pmatrix} \sigma^{00} \\ \sigma^{01} \\ \sigma^{11} \end{pmatrix} \quad (12)$$

The eigenvalues of this 3×3 matrix can be used for further analysis.

Irreducible Minkowski tensors

The redundancy of the Cartesian representation can be entirely avoided by the so-called irreducible Minkowski tensors (IMT). This representation expands the MT in spherical harmonics so that a tensor of rank s only captures s-fold anisotropy. In other words, the MT are decomposed according to their symmetry.

In Euclidean space, they are obtained by calculating a normal vector density for a shape. This density describes what fraction of the body's normal vectors point in which direction. In the plane, these directions are distributed on $[0, 2\pi)$. The Fourier coefficients of the density of normal vectors are called IMT and have been used in two dimensions (2D)[5,44,45], and in 3D[46–48]. A full set of IMT for a convex shape will completely describe the shape. The IMT are complex scalars. They provide a natural way to characterize both the degree of anisotropy and directional information for any rank via their phase and absolute value. Such a scalar representation is essential for higher orders, where Cartesian tensors become unwieldy. A tangible demonstration of their meaning can, e.g., be found in Figs. 1 and 2 of Collischon et al.[44].

Here, we define IMT for the first time to our knowledge on the sphere. Note that a simple embedding in 3D fails to distinguish isotropic from anisotropic bodies on the sphere. For example, a spherical cap is an isotropic body on the sphere, but IMT of an embedding in 3D would, undesirably, assign to it a high degree of anisotropy. The solution is to parallel transport the normal vectors to a single point, where they can then be treated as in the Euclidean plane (i.e., calculating their angular density). This suitable representation provides a powerful characterization of spherical anisotropy, as demonstrated below. Hence, this definition is an important step towards an effective shape analysis on the sphere for anisotropies and symmetries of arbitrary rank.

Let ρ_K be the normal density of a body K, where the functional value $\rho_K(\varphi)$ is proportional to the portion of the body's contour that points into the direction φ. The total integral equals the contour length of the boundary ∂K. For a spherical polygon (such as any shape defined by pixelated images on a sphere), the normal density can be written as

$$\rho_K(\varphi) = \sum_k L_k \, \delta(\varphi - \varphi_k) \quad (13)$$

where the edges are indexed by k, have lengths L_k, and orientations φ_k. On the sphere, φ is determined from the direction of the normal vector $\mathbf{n}$ parallel transported to a common point. We choose 0 to represent south, and $\pi/2$ east.

The IMT are then obtained by Fourier transforming ρ_K:

$$\psi_b(K) = \int_0^{2\pi} \mathrm{e}^{\mathrm{i}b\varphi} \rho_K(\varphi) \, \mathrm{d}\varphi \overset{\text{polygon}}{=} \sum_k L_k \mathrm{e}^{\mathrm{i}b\varphi_k} \quad (14)$$

The absolute values $|\psi_b(K)|$ of the IMT are then useful measures for the degree of anisotropy with respect to b-fold symmetries. Furthermore, the corresponding preferred directions are given by $\varphi_n = (2\pi n + \arg(\psi_b))/b$ where $n \in \{0, \ldots, b-1\}$.

Calculating Minkowski maps

Localized MT for grayscale images are calculated in the form of Minkowski maps (MM) using local observation windows. In Euclidean space, code is available in the papaya2[49] and the related banana[44] libraries, the latter refining the former for astronomical image analysis. We adapt those techniques for squares in the Euclidean plane on the sphere using the HEALPix scheme (Hierarchical Equal Area isoLatitude Pixelation, https://healpix.sourceforge.io)[50], see Fig. 2a). This scheme is commonly used for CMB data and further described in Methods section. The body to be described by the tensors is obtained by choosing a brightness threshold, treating everything above as part of the body. Our implementation, `litchi`, is publicly available[30].

Our scheme is based on a marching square algorithm. First, a window of (usually) 2×2 pixels is selected by choosing all pixels that meet in one corner, using the pixel centers as the corners of the window. At eight positions in HEALPix, only three pixels meet in a triangular shape, which is treated conceptionally identically and is only a special case in the implementation wherever the explicit number of pixels matters. Two examples for this can be seen in Fig. 2a). All such neighborhoods together form a marching square grid, as explained in more detail in the methods section. Each pixel value is then either above or below the given threshold, yielding 16 possible cases of black-and-white neighborhoods, shown in Fig. 2b).

These configurations define how the contour segment passes through the window, where we assume these segments to be geodesics. Their endpoints at the edge of the window are interpolated between the neighboring pixel centers depending on the threshold and pixel values using a known technique[51], also shown in Fig. 2c). The diagonal cases are chosen to be connected or disconnected based on the total average[52].

Let α be the angular distance between both pixel centers, denoted by A and B. Let t be the chosen brightness threshold, and p_A and p_B be the pixel values at A and B respectively. Then the angular distance d from A to the contour in the direction of B is given by

$$d = \alpha \frac{t - p_A}{p_B - p_A}. \quad (15)$$

The normal vector pointing away from the body in tangential space is then calculated for the window. Since these segments are short, a zeroth-order approximation for the integral is used, where the length of the segment is simply multiplied by the tensorial integrand[41].

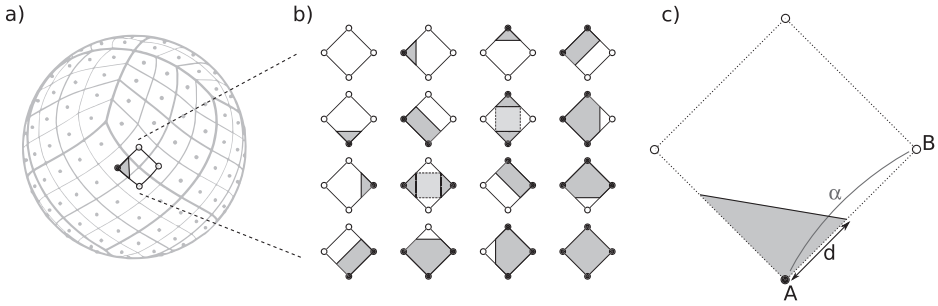

Fig. 2 | The computation of a marching square on HEALPix. a Position of a marching square window within the HEALPix grid (HEALPix background image vectorized from Martinez-Castellanos et al.[81], Fig. 1c, CC BY 4.0). **b** Possible configurations of a 2×2 pixel-window. The small circles represent pixel centers that are either below (open) or above (filled) a certain threshold. The union of gray areas approximates the unpixelated shape within the observation window. In the diagonal cases, the corners are assumed to be disjoint if the total average lies below the threshold, and connected otherwise[52]. **c** Interpolation of a contour segment (solid line) between pixel centers, where A marks the center of a pixel above the threshold, and the other circles mark pixel centers below the threshold. The point where the interpolated contour lies between two pixel centers is calculated according to Eq. (15). Here, α is the angular distance from A to B and d the angular distance from A to the interpolated contour in that direction.

Note that the EVQ of $W_1^{0,2}$ of such a short straight line will diverge as one of the eigenvalues goes to zero. To avoid this divergence and, more importantly, to access structural information over an extended area, we used larger windows on top of the 2×2 marching squares. The locally calculated segment-tensors are parallel transported to the center of this enlarged window and then summed up. Each large window should contain enough contour segments at various angles to allow for a sensible analysis. Finally, one can use an output map at lower resolution to depict the results, where pixel centers correspond to the centers of the larger windows.

This procedure uses a single threshold, which may be an insufficient representation of the structure. For a more comprehensive analysis, we can add up tensors that are calculated for contours at several thresholds before smoothing to portray the data as accurately as necessary. Compared to a previous method implemented by Goyal et al.[53], where localized structural information was only calculated at specific pixelation-dependent scales and positions, MM provide a more versatile approach. Further implementation details can be found in the methods section.

Test cases

For demonstration purposes, we generated MM for several exemplary shapes. All shapes occupy only a few degrees around the equator to keep spherical effects small and the results intuitive.

Rank 2. We begin with the EVQ of $W_1^{0,2}$ and $|\psi_2|$ of a square and two rectangles with aspect ratios 2:1 and 3:1 respectively. The corresponding MM are shown together with the input shape and the moving window size in Fig. 3a, b; see the panels at the top, left and right, and the bottom left panels. Near the origin, all shapes are entirely contained within the window, and the anisotropy depends on the aspect ratio; the EVQ is an explicit function of the aspect ratio. When the window is moved sideways, the respective opposite side of the rectangle moves out of the window; hence, the anisotropy increases. Even further away from the center, the anisotropy decreases as the remaining sides at the top and bottom get shorter and cancel out with the nearest edge. Finally, only one side (and increasingly shorter sections thereof) is left in the window, leading to a diverging EVQ while $|\psi_2|$ remains low. If only a corner is left in the window, the EVQ is close to one, and $|\psi_2|$ is close to zero as two perpendicular contours have no two-fold anisotropy. The same test was done for a cross; see Fig. 3a, b, bottom right panels. Now, the anisotropy is low as long as most of the shape is within the window, except if only one bar is within the window. From that point on, the map exhibits the same patterns as for the rectangles.

As expected, very high values in the Cartesian maps signify that only a part of the shape is within the window. Larger windows relative to the shapes smooth out these edge effects because the relative area on the MM where the window contains the whole shape increases with the window size, whereas regions where edge effects prevail depend on the size of the shape. For an extended pattern such as the CMB temperature distribution, the window size needs to be large enough compared to a characteristic length scale to avoid diverging border effects. Even larger windows can be used to check the relative alignment of the shapes making up the pattern. Such a choice corresponds to analyzing the whole cross as opposed to a single bar.

Care needs to be taken near masked regions where only a few contour segments may be left in an otherwise sufficiently large window. We, therefore, only allow a small fraction ($< 1/16$) of input pixels in a window to be masked, treating the whole window as masked otherwise. More details on our masking can be found in the methods section.

Rank 4. While rank 2 MT encode information about elongation (2-fold symmetry), rank 4 MT contain information about 4-fold symmetry ("squareness"). We have tested various options to depict $W_1^{0,4}$ using the eigenvalues of the matrix in Eq. (12); for more details, see the methods section. The most useful choice for our shape analysis turned out to be the tensor's mid eigenvalue (i.e., its second largest eigenvalue). Maps using this measure and $|\psi_4|$ of the same example shapes as above are shown in Fig. 3c, d.

Threshold dependent graphs. Additional information about the structure in a grayscale image with more than just black-and-white pixels can be gained by varying the brightness threshold, which changes the shape of the contours. The chosen shape measure can then be plotted as a function of the brightness threshold. This procedure is an established way to apply the MF/MT to data that has been used in many previous works[9,10,22,28,45].

MT analysis applied to Planck data

Next, we use our methods developed above to analyze real CMB data, specifically Planck temperature data. More details and explanations regarding the basics of Planck data products and analysis are given in the methods section.

In our analysis, we calculate MM of the EVQ of $W_1^{0,2}$ for 13 thresholds between -3 and 3 standard deviations. Contours for all thresholds are combined in each MM. We use Planck PR3 CMB SMICA temperature data and 999 FFP10 simulations at $N_{\mathrm{side}} = 512$, smoothed with FWHM$= 20'$, and a MM window radius of 6°. We, moreover, use the Common Mask (also at $N_{\mathrm{side}} = 512$ and smoothed with FWHM$= 20'$, setting all pixels above

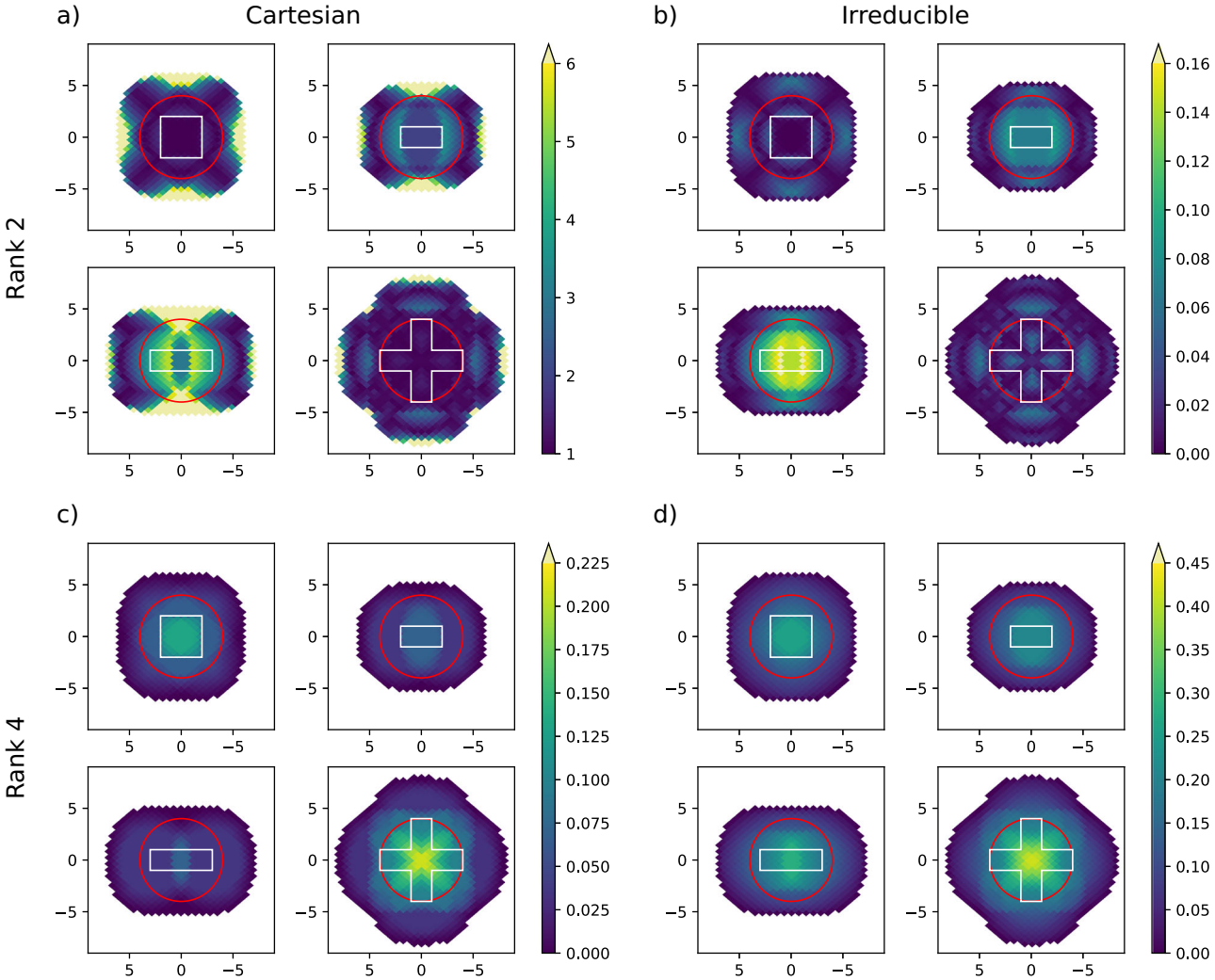

Fig. 3 | Minkowski maps of rank 2 and 4 anisotropy measures of a square, elongated rectangle, longer rectangle, and cross. a Using the eigenvalue quotient of $W_1^{0,2}$. **b** Using $|\psi_2|$. **c** Using the mid eigenvalue of $W_1^{0,4}$. **d** Using $|\psi_4|$. Each white contour depicts the shape of the (input) body, and the red circles indicate the window size. Coordinates are given in degrees. Input N_{side} was 512 and that of the output 128.

0.95 to unmasked), and N_{side} of the output MM is 16. Since the MM window radius is larger than the output pixel size, each output pixel describes its local surroundings, avoiding divergences due to a lack of contours in the window. As above, we took the (pointwise) mean and standard deviation of the simulation MM and used these to estimate the local deviation from the data; see Fig. 4a and b. We also tested smoothing the MM again, after calculating the scalar map, to check for larger-scale deviations in anisotropy at this scale; see Fig. 4a, c, e for unsmoothed and b, d, f for smoothed data.

Our analysis identifies two spots of interest: one close to $(l_1, b_1) = (225, -69)$ and one near $(l_2, b_2) = (80, 27)$, which are highlighted by red marks in the temperature map of Fig. 5. The first spot is close to the so-called Cold Spot at around $(l, b) = (210, -57)$, an anomaly first detected in data by the WMAP mission[31,54,55] and later also in Planck data[56,57]. However, the distance of (l_1, b_1) to the Cold Spot is slightly larger than the window diameter, which suggests that these spots are statistically independent. For both (l_1, b_1) and (l_2, b_2), the data map shows a deviation in anisotropy compared to the simulations by more than 4σ. A third spot near $(l_3, b_3) = (337, 62)$ reaches similar values as (l_1, b_1) in the unsmoothed maps, but lower values when using smoothed maps. Here, just a single pixel in the region reaches high values, as opposed to the more extended regions around the other two spots. We will thus regard it as less notable than the other two and focus on (l_1, b_1) and (l_2, b_2).

The MM pixel values do not follow a Gaussian distribution, so units of standard deviation are not an ideal measure of deviation. Better measures are the local and global percentile of the data and the simulations, that is, the fraction of simulation MM pixels that take a lower value than the given data MM pixel. These percentiles can be evaluated either pointwise (comparing pixels at the same positions) or globally (comparing each data pixel to all simulation pixels). The results are shown in Fig. 4c, d, e, and f. The local method has the advantage that it takes pixel distortion into account, whereas the global method provides better statistics. Using only the local method has the risk of comparing an outstanding point in the data to an average point in the simulations, ignoring similar points. Both the local and global analyses find the same two spots at percentile values >99%.

For a better understanding of the global significance of these values, we performed a simple evaluation of the look-elsewhere-effect. We counted the amount of simulation maps that contain at least one higher MM pixel value than each (unsmoothed) data MM pixel. The value at (l_2, b_2) is only surpassed by 6 simulations, making it quite outstanding. For (l_1, b_1), 943 out of 999 simulations surpass the data value in at least one pixel, making it seem not very significant. One caveat of this analysis is that it does not take pixel distortion and correlations into account. Additionally, (l_1, b_1) is compared to the highest spots in the simulation maps, despite not being the highest region in the data. Simply taking the second or third highest pixels in each

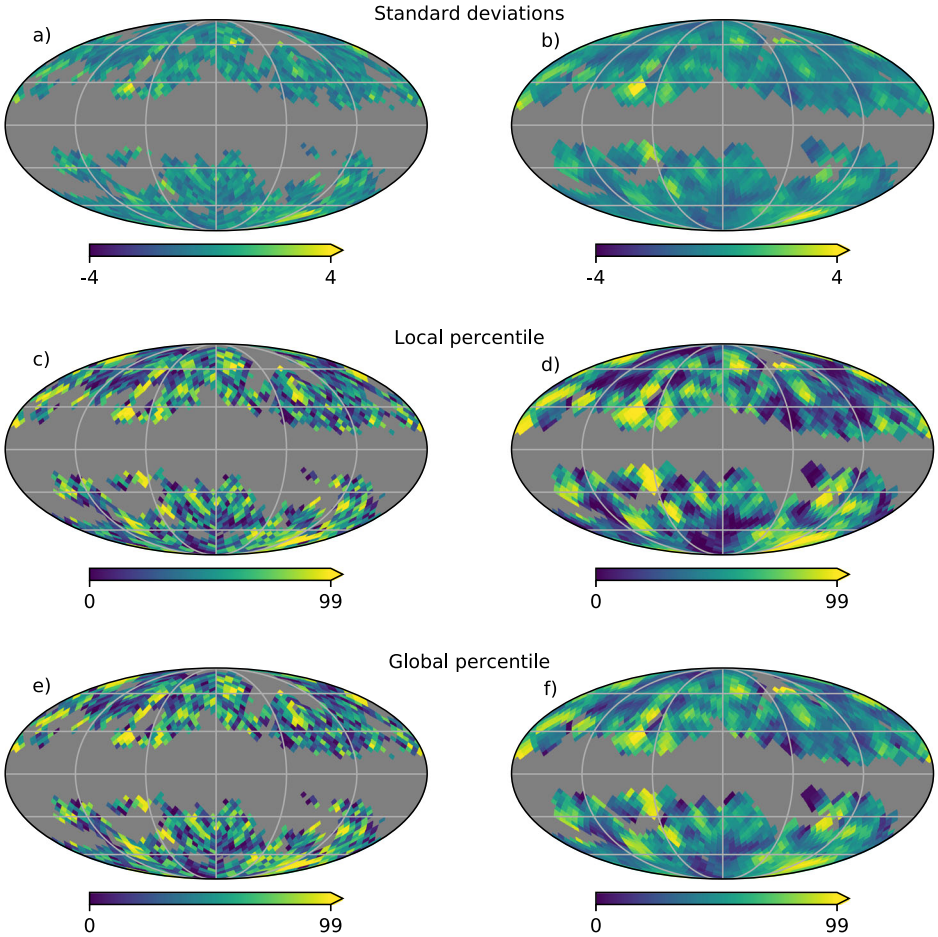

Fig. 4 | Deviation between SMICA temperature data and simulations via the eigenvalue quotient of $W_1^{0,2}$. We used a window size of 6° and masked the data with the Common Mask (gray areas). The deviation was calculated using various methods: **a**, **c**, **e** no smoothing of the Minkowski maps before calculating the deviation; **b**, **d**, **f** Minkowski maps smoothed with FWHM 6°. Deviation is shown as: **a**, **b** multiples of local standard deviation **c**, **d** local percentiles; **e**, **f** global percentiles, where percentiles refer to the amount of simulation pixels with values below a given data pixel. High values stand for high 2-fold anisotropy of the temperature data.

simulation would not be sufficient as those might be correlated and located right next to the highest pixel. These numbers must thus be taken with a grain of salt.

The spots are also identified using PR3 data and 999 simulations by the Commander pipeline and when using the absolute values of irreducible tensors of rank 2 instead of the EVQ of $W_1^{0,2}$. For Commander, the standard deviation of the simulation MM pixels is larger, which naturally results in a smaller multiple of standard deviation. However, we still obtain high percentile values (>97% global smoothed MM, > 99% global unsmoothed and local MM). Varying the window size by about 10% gives qualitatively the same results. The spot (l_2, b_2) is located near a masked region in the MM, which is due to several smaller masked spots [see Supplementary Fig. 1 in SI and compare to Supplementary Fig. 2 depicting (l_1, b_1)], but we assume that those masked areas do not significantly change the result since they are cut out rigorously. Furthermore, the window contains enough contours to exclude edge effects; see the methods section for further details on masking.

To see whether the analysis is affected by the aforementioned non-contour-preserving properties of the HEALPix grid, (l_1, b_1) and (l_2, b_2) are rotated to the center of the coordinate system, and the MM of the data is recalculated. The deviation there is slightly smaller but still remarkable (>3.5σ/ >99.4% for (l_1, b_1); >4.4σ/ >99.9% for (l_2, b_2); using unsmoothed MM and for both percentiles).

Looking into those regions with threshold-dependent graphs using 600 SMICA simulations, we find that the southern spot at (l_1, b_1) exceeds 99% of the simulations (local percentile), whereas the other spot does not. The excess in the map of all thresholds combined probably occurs due to correlations between maps calculated for several different single thresholds so that it exceeds in total but not for a single threshold.

Note that, in a similar analysis, Joby et al.[28] also analyzed Planck temperature data by calculating the eigenvalue ratio of $W_1^{0,2}$ with a different method based on covariant derivatives of the field. They took a global approach, integrating over the whole sphere at once at various (single) thresholds ranging from −3 to 3 standard deviations of brightness for each map. Thus, the EVQ can be plotted as a function of the brightness threshold. Using the Planck CMB temperature map given by the SMICA component separation pipeline and 100 FFP8 simulations at a resolution of $N_{\mathrm{side}} = 512$ (all smoothed with FWHM=20′ and masked with the Common Mask), they find good agreement between data and simulations.

For a better comparison to Joby et al.[28], we created threshold dependent graphs of the whole sky. For this purpose, we used MM with a window size of 6 and 10 degrees and averaged globally for each threshold. The data is around the 1st percentile of the simulations, making it more isotropic than the average simulation. These results are clearly an interesting confirmation of isotropy and comparable to the results of Joby et al.[28], who found a similar alignment of structures looking at only the 30 GHz channel, probably due to beam effects.

To look into larger structures, we created MM with a window radius of 30 degrees and the same parameters as above. Due to masking, only caps around the polar regions remain to be analyzed. The data stays below 98.5% of the simulations both locally and globally.

For a more comprehensive shape analysis of the two anomalous regions and the Cold Spot, we also performed a multivariate analysis that combines anisotropy of different ranks. Therefore, we created scatter plots that show the anisotropy of ranks 2 and 4 for the MM pixels, which are based on the IMT. To highlight outliers, the scatter plots compare the results of simulations and data. Figure 6 shows one scatter plot for each region. Importantly, the anisotropy information of the two different ranks appears

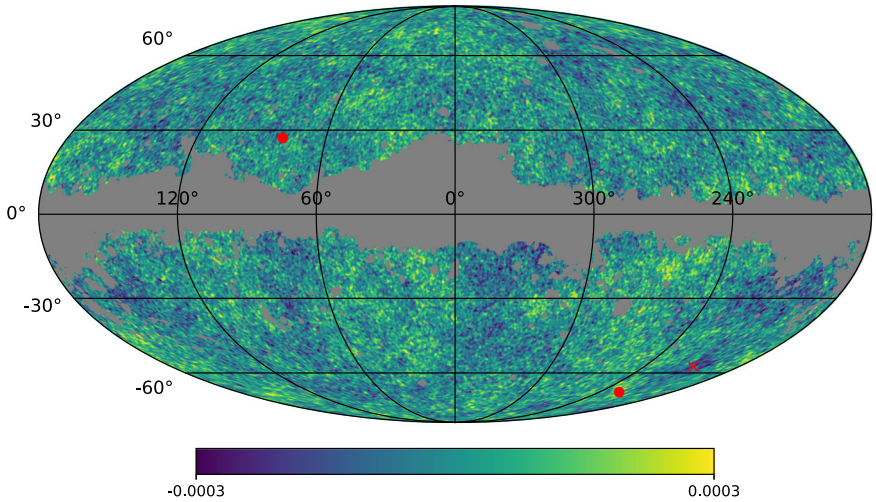

Fig. 5 | SMICA PR3 cosmic microwave background temperature map. Markings show the detected anomalous regions (red dots) and the Cold Spot (red cross). Gray areas are masked with the Common Mask. $N_{side} = 512$.

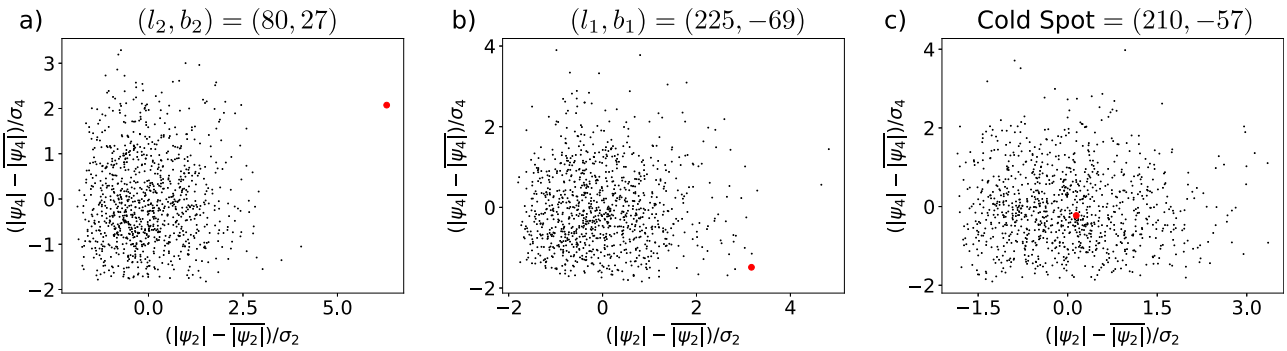

Fig. 6 | Scatter plots showing irreducible anisotropy at ranks 2 and 4 for single Minkowski map pixels. Pixels shown are located at $(l_2, b_2) = (80, 27)$ **a**, the region next to the Cold Spot $(l_1, b_1) = (225, -69)$ **b**, and at the Cold Spot at $(210, -57)$ **c**. Small black dots show pixels in the simulations; large red dots show data pixels.

to be independent — by virtue of our irreducible representation. For the Cold Spot, the data lies well within the simulations; for the spot close by, i.e., (l_1, b_1), the rank 2 IMT exceed most simulations, but not the rank 4 IMT. Only for the spot at (l_2, b_2) do we find that both rank 2 and 4 IMT are distinctly larger for the data than for any of the simulations. None of the spots are noteworthy if we only use $|\psi_4|$. The Cold spot does not appear noteworthy in the MM because we analyze its shape and not absolute value information. Hence, our analysis provides information that is complementary to that of classical methods.

Discussion

We propose a new framework for shape analysis on the sphere using Cartesian and irreducible Minkowski tensors. We, specifically, devised an irreducible representation on the sphere to gain access to higher-rank tensors. We, moreover, introduced MM to the sphere, implementing parallel transport. The MM provide a path for a localized analysis at any given scale of interest. Adaptation to interdisciplinary fields of research is facilitated by our open-source software `litchi`. Previous open software on the sphere only incorporated the global MF[25,58]; to our knowledge no tools for calculating any MT on the sphere are available to the public and no such local analysis has been done by other groups. `litchi` is not only the first available open-source tool for calculating MF and MT on the sphere using MM known to us, it also provides access to arbitrary rank via the IMT.

We applied these tools to CMB data, finding noteworthy spots in CMB temperature data. One of them is near the Cold Spot, the other above the Galactic plane. Next, a more elaborated analysis is needed to disentangle the nature and origin of the anomalies detected here. Such an analysis is beyond the scope of this paper, where we present the general framework of Minkowski tensors on the sphere.

Several possible origins for anisotropy have been suggested in the literature and the following is a non-exhaustive list. Cosmic strings, 1D topological defects caused by symmetry breaking in the early universe[59], have been considered as a potential source for anomalies in the shape of temperature discontinuities[60]. Constraints on their parameters are found in gravitational wave data[61–63]. Another possible avenue is (global) cosmic topology. Nontrivial topologies of spacetime caused by quantum processes may lead to correlations observable in the CMB that have not been ruled out yet (see e.g., Akrami et al.[64] and references therein). The homogeneous and anisotropic Bianchi models are another approach to anisotropy, see e.g., Ellis[65] for a review. There, the isotropic FLRW metric is replaced by anisotropic alternatives.

In summary, we provide a generic toolset for anisotropy on the sphere that can be applied to any spherical data set with manifold conceivable applications. We mention exemplarily the characterization of patterns in earth observation data[66], for climate research (like teleconnection patterns induced by El Niño-Southern Oscillation (ENSO)[67,68]), heterogeneous pattern on cell surfaces (e.g., patches of highly adhesive proteins[69]), or emergence phenomena of active matter on the sphere[70–73], where the role of a non-Euclidean geometry on self-organization is not yet understood.

In these and many other cases, MT as shape descriptors that capture n-point information will likely give new insights into the phenomenologies and their underlying governing rules.

Methods

Basics of Planck data analysis

Planck data maps are given in the HEALPix format[50], for which software packages in various languages are provided. A multitude of Planck data products are available in the Planck Legacy Archive[74,75], including component-separated temperature and polarization maps generated with different pipelines[76] and simulations thereof[77]. Additional information can be found in the Planck Explanatory Supplement.

Within HEALPix, pixels can be ordered using a ring-wise (RING) or a nested (NEST) scheme. The execution speed of some functions may depend on this. For use with `litchi`, nested ordering is faster. The pixel size is characterized by the N_{side} parameter which gives the number of pixels as $N_{\mathrm{tot}} = 12N_{\mathrm{side}}^2$. The maximum resolution available is usually $N_{\mathrm{side}} = 2048$ (corresponding to a pixel radius of up to 1.8'). Downgrading to a lower resolution is usually done by transforming into harmonic space. Since pixels represent an average of the field where they are located, pixel window functions need to be taken into account (which are provided and implemented in healpy's `pixwin` function). We set $l_{\mathrm{max}} = 3\,N_{\mathrm{side,out}} - 1$ and $m_{\mathrm{max}} = l_{\mathrm{max}}$ as spherical harmonics on HEALPix are linearly independent up to this value[78]. The harmonic coefficients are then deconvolved with the previous beam size (5′ for $N_{\mathrm{side}} = 2048$), convolved with a larger window (20′ for $N_{\mathrm{side}} = 512$), and transformed back to real space at a lower resolution. These window sizes are typical for Planck data[22].

Marching squares on HEALPix

The marching square procedure gives the tensors in a grid whose pixel centers are located at the intersections of the original HEALPix grid pixels and whose corners are at the original pixel centers. The result is not a HEALPix grid. We implemented this MM-grid by assigning each MM pixel the number of the HEALPix pixel to its east (so each HEALPix-pixel number refers to the western corner of that pixel). This procedure is demonstrated for an exemplary pixel in Supplementary Fig. 3. Note that this technique cannot be applied to the poles. Hence, we assigned special negative numbers to the poles in the MM-grid.

Contours are distorted on the HEALPix grid. This effect is visible when looking at the average neighbor distance of each pixel (Supplementary Fig. 4). The distorted pixel shapes affect the contour length when looking at small, pixel scale structures, but the effect is less prominent for larger objects. Our tests found that rotating areas of interest to the origin did not significantly change the deviation between data and simulations. Since data and simulations are equally affected, we chose to neglect this effect.

Parallel transport in `litchi` is implemented as a single step in the Schild's ladder procedure (introduced by Alfred Schild in lectures at Princeton University, presented by Misner et al.[79]). A recursive scheme enabling several steps was tested and made no significant difference over the relevant angular distances.

Masks can be applied to the image in `litchi` by giving a HEALPix-file of the same N_{side} and numbering scheme as the data to be analyzed. The mask is expected to take values between zero and one, and a threshold is applied (default: 0.9). Any pixel below this value is assumed to be masked and set to NAN (not a number) in the data. No contours touching a masked area are included in the further analysis. If more than 1 in 16 pixels contributing to an output MM pixel are masked, the output pixel is set to NAN.

Rank 4 Anisotropy measures

On the path to an anisotropy measure on rank 4, we tried several possibilities. The first ansatz is to use the norm of a vector containing the eigenvalues and is shown in Supplementary Fig. 5. The results look very similar to simply calculating the area of the shape in the window.

Next, we can look at the three eigenvalues directly. Figure 3c, Supplementary Figs. 6 and 7 show the largest to smallest eigenvalue of the example shapes, respectively. While the largest eigenvalue again looks similar to the first ansatz, the other two apparently encode 4-fold symmetry information, reaching higher values for the cross and square.

To better distinguish between the effects of the smallest and middle eigenvalue, we generated the same images using a triangle and a parallelogram. While the smallest eigenvalue reaches high values for these new shapes compared to the former examples (Supplementary Fig. 8, bottom), the other one does not react to them in a strong way (Supplementary Fig. 8, top). Note that the diagonal lines are pixelated and not as smooth as shown in the examples, but this does not introduce a 4-fold symmetry. Based on these tests, we decide that the middle eigenvalue of $W_1^{0,4}$ as represented in Eq. (12) is a useful measure of 4-fold symmetry.

Data availability

The data and simulations used in this work are publicly available in the Planck Legacy Archive[74]. Further data products were generated with `litchi` with the parameters stated in the text and are available from C.C. on reasonable request.

Code availability

The MM generation procedure was implemented in `litchi`, which is a lightweight tool written in C++. Python bindings are included to allow for Python-only analysis scripts and its header-only structure allows for an easy integration with other C++-based projects. It is available at https://github.com/ccollischon/litchi[30].

Received: 9 February 2024; Accepted: 18 July 2024;
Published online: 27 July 2024

References

1. Chiu, S. N., Stoyan, D., Kendall, W. S. & Mecke, J. *Stochastic geometry and its applications* (John Wiley & Sons, 2013).
2. Schneider, R. & Weil, W. *Stochastic and Integral Geometry* (Springer, 2008).
3. Kerscher, M. Non-Gaussian morphology on large scales: Minkowski functionals of the REFLEX cluster catalogue. *AA* **377**, 1–16 (2001).
4. Räth, C. et al. Comparing the sensitivity of wavelets, minkowski functionals and scaling indices to higher order correlations in mr images of the trabecular bone using surrogates. *J.P.W. Pluim, B.M. Dawant: Medical Imaging 2009: Image Processing, Society of Photo-Optical Instrumentation Engineers* **7259**, 1–10 (2009).
5. Klatt, M. A., Schröder-Turk, G. E. & Mecke, K. Mean-intercept anisotropy analysis of porous media. II. Conceptual shortcomings of the MIL tensor definition and Minkowski tensors as an alternative. *Med. Phys.* **44**, 3663–3675 (2017).
6. Räth, C. Strength through structure: visualization and local assessment of the trabecular bone structure. *N. J. Phys.* **10**, 125010 (2008).
7. Rahman, N. & Shandarin, S. F. Measuring shapes of galaxy images - II. Morphology of 2MASS galaxies. *MNRAS* **354**, 235–251 (2004).
8. Böbel, A. & Räth, C. Kinetics of fluid demixing in complex plasmas: domain growth analysis using minkowski tensors. *Phys. Rev. E* **94**, 013201 (2016).
9. Schröder-Turk, G. E. Minkowski tensor shape analysis of cellular, granular and porous structures. *Adv. Mater.* **23**, 2535–2553 (2011).
10. Göring, D., Klatt, M. A., Stegmann, C. & Mecke, K. Morphometric analysis in gamma-ray astronomy using Minkowski functionals. Source detection via structure quantification. *AA* **555**, A38 (2013).
11. Klatt, M. A. & Mecke, K. Detecting structured sources in noisy images via minkowski maps. *Europhys. Lett.* **128**, 60001 (2020).
12. Schuetrumpf, B. Appearance of the single gyroid network phase in "nuclear pasta" matter. *Phys. Rev. C.* **91**, 025801 (2015).
13. Böbel, A., Knapek, C. & Räth, C. Scale-free crystallization of two-dimensional complex plasmas: Domain analysis using minkowski tensors. *Phys. Rev. E* **97**, 053201 (2018).
14. Rocha, G., Hobson, M. P., Smith, S., Ferreira, P. & Challinor, A. Simulation of non-Gaussian cosmic microwave background maps. *Monthly Not. R. Astronom. Soc.* **357**, 1–11 (2005).

15. Elsner, F. & Wandelt, B. D. Improved simulation of non-gaussian temperature and polarization cosmic microwave background maps. *Astrophys. J. Suppl. Ser.* **184**, 264 (2009).
16. Planck Collaboration IX. Planck 2015 results - IX. Diffuse component separation: CMB maps. *AA* **594**, A9 (2016).
17. Gott J. R. III et al. Topology of microwave background fluctuations: theory. *ApJ* **352**, 1–14 (1990).
18. Colley, W. N., Gott III, J. R. & Park, C. Topology of COBE microwave background fluctuations. *MNRAS* **281**, L82–L84 (1996).
19. Schmalzing, J. & Gorski, K. M. Minkowski functionals used in the morphological analysis of cosmic microwave background anisotropy maps. *MNRAS* **297**, 355–365 (1998).
20. Ducout, A., Bouchet, F. R., Colombi, S., Pogosyan, D. & Prunet, S. Non-Gaussianity and Minkowski functionals: forecasts for Planck. *Monthly Not. R. Astronomical Soc.* **429**, 2104–2126 (2012).
21. Duque, J. C. & Marinucci, D. Geometric methods for cosmological data on the sphere. *Annu. Rev. Stat. Its Application* **11**, null (2024).
22. Planck Collaboration VII. *Planck* 2018 results. VII. Isotropy and statistics. *AA* **641**, A7 (2020).
23. Komatsu, E. Hunting for primordial non-Gaussianity in the cosmic microwave background. *Classical Quantum Gravity* **27**, 124010 (2010).
24. Modest, H. Scale-dependent non-gaussianities in the cmb data identified with minkowski functionals and scaling indices. *Monthly Not. R. Astronomical Soc.* **428**, 551–562 (2013).
25. Carones, A., Duque, J. C., Marinucci, D., Migliaccio, M. & Vittorio, N. Minkowski functionals of CMB polarization intensity with Pynkowski: Theory and application to Planck and future data. *Monthly Not. R. Astronomical Soc*. **527**, 756–773 (2023).
26. Chingangbam, P. & Rahman, F. Minkowski functionals for composite smooth random fields. *Phys. Rev. D.* **109**, 083530 (2024).
27. Chingangbam, P. Tensor Minkowski Functionals for random fields on the sphere. *J. Cosmol. Astropart. Phys.* **2017**, 023 (2017).
28. Joby, P. K., Chingangbam, P., Ghosh, T., Ganesan, V. & Ravikumar, C. D. Search for anomalous alignments of structures in Planck data using Minkowski tensors. *J. Cosmol. Astropart. Phys.* **2019**, 009 (2019).
29. Appleby, S., Kochappan, J. P., Chingangbam, P. & Park, C. Minkowski tensors in redshift space-beyond the plane-parallel approximation. *ApJ* **942**, 110 (2023).
30. Collischon, C. ccollischon/litchi: Initial release https://doi.org/10.5281/zenodo.11940174 (2024).
31. Vielva, P., Martínez-González, E., Barreiro, R. B., Sanz, J. L. & Cayón, L. Detection of non-Gaussianity in the Wilkinson microwave anisotropy probe first-year data using spherical wavelets. *ApJ* **609**, 22–34 (2004).
32. Schröder-Turk, G., Kapfer, S., Breidenbach, B., Beisbart, C. & Mecke, K. Tensorial Minkowski functionals and anisotropy measures for planar patterns. *J. Microsc.* **238**, 57–74 (2010).
33. Adler, R. J. & Taylor, J. E. *Random Fields and Geometry* (Springer-Verlag, New York, 2007).
34. Matsubara, T. & Kuriki, S. Weakly non-Gaussian formula for the Minkowski functionals in general dimensions. *Phys. Rev. D.* **104**, 103522 (2021).
35. Gay, C., Pichon, C. & Pogosyan, D. Non-Gaussian statistics of critical sets in 2D and 3D: peaks, voids, saddles, genus, and skeleton. *Phys. Rev. D.* **85**, 023011 (2012).
36. Fantaye, Y., Marinucci, D., Hansen, F. & Maino, D. Applications of the Gaussian kinematic formula to CMB data analysis. *Phys. Rev. D.* **91**, 063501 (2015).
37. Hadwiger, H. *Vorlesungen Über Inhalt, Oberfläche und Isoperimetrie* (Springer, Berlin Heidelberg, 1957).
38. Klain, D. & Rota, G. *Introduction to Geometric Probability*. (Cambridge University Press, 1997).
39. Alesker, S. Description of continuous isometry covariant valuations on convex sets. *Geometriae Dedicata* **74**, 241–248 (1999).
40. Schröder-Turk, G. E. Minkowski tensors of anisotropic spatial structure. *N. J. Phys.* **15**, 083028 (2013).
41. Fabian, W. Tensor integrals. *Proc. Edinb. Math. Soc.* **10**, 145–151 (1957).
42. Kochappan, J. P., Sen, A., Ghosh, T., Chingangbam, P. & Basak, S. Application of the contour minkowski tensor and $\mathcal{D}$ statistic to the planck *e*-mode data. *Phys. Rev. D.* **103**, 123523 (2021).
43. Mehrabadi, M. M. & Cowin, S. C. Eigen tensors of linear anisotropic elastic materials. *Q. J. Mech. Appl. Math.* **43**, 15–41 (1990).
44. Collischon, C., Sasaki, M., Mecke, K., Points, S. D. & Klatt, M. A. Tracking down the origin of superbubbles and supergiant shells in the Magellanic Clouds with Minkowski tensor analysis. *AA* **653**, A16 (2021).
45. Klatt, M. A., Hörmann, M. & Mecke, K. Characterization of anisotropic Gaussian random fields by Minkowski tensors. *J. Stat. Mech.* **2022**, 043301 (2022).
46. Kapfer, S. C.*Morphometry and Physics of Particulate and Porous Media*. Ph.D. thesis, Friedrich-Alexander-Universität Erlangen-Nürnberg (2011).
47. Kapfer, S. C., Mickel, W., Mecke, K. & Schröder-Turk, G. E. Jammed spheres: Minkowski tensors reveal onset of local crystallinity. *Phys. Rev. E* **85**, 030301 (2012).
48. Mickel, W., Kapfer, S. C., Schröder-Turk, G. E. & Mecke, K. Shortcomings of the bond orientational order parameters for the analysis of disordered particulate matter. *J. Chem. Phys.* **138**, 044501 (2013).
49. Schaller, F. M., Wagner, J. & Kapfer, S. C. papaya2: 2d irreducible minkowski tensor computation. *J. Open Source Softw.* **5**, 2538 (2020).
50. Górski, K. M. HEALPix: A Framework for High-Resolution Discretization and Fast Analysis of Data Distributed on the Sphere. *ApJ* **622**, 759–771 (2005).
51. Mantz, H., Jacobs, K. & Mecke, K. Utilizing Minkowski functionals for image analysis: a marching square algorithm. *J. Stat. Mech.: Theory Exp.* **2008**, P12015 (2008).
52. Appleby, S. Minkowski Tensors in Two Dimensions: Probing the Morphology and Isotropy of the Matter and Galaxy Density Fields. *ApJ* **858**, 87 (2018).
53. Goyal, P. & Chingangbam, P. Local patch analysis for testing statistical isotropy of the planck convergence map. *J. Cosmol. Astropart. Phys.* **2021**, 006 (2021).
54. Cruz, M., Martínez-González, E., Vielva, P. & Cayón, L. Detection of a non-Gaussian spot in WMAP. *MNRAS* **356**, 29–40 (2005).
55. Vielva, P. A Comprehensive Overview of the Cold Spot. *Adv. Astron.* **2010**, 592094 (2010).
56. Planck Collaboration XXIII. *Planck* 2013 results. XXIII. Isotropy and statistics of the CMB. *AA* **571**, A23 (2014).
57. Planck Collaboration XVI. *Planck* 2015 results. XVI. Isotropy and statistics of the CMB. *AA* **594**, A16 (2016).
58. Hamann, J. & Kang, Y. A Minkowski functional analysis of the Cosmic Microwave Background weak lensing convergence. *J. Cosmol. Astropart. Phys.* **2024**, 076 (2024).
59. Kibble, T. W. B. Topology of cosmic domains and strings. *J. Phys. A: Math. Gen.* **9**, 1387 (1976).
60. Planck Collaboration XXV. *Planck* 2013 results. XXV. Searches for cosmic strings and other topological defects. *AA* **571**, A25 (2014).
61. EPTA Collaboration. The second data release from the European Pulsar Timing Array. IV. Implications for massive black holes, dark matter, and the early Universe. *AA* **685**, A94 (2024).
62. Abbott, B. P. All-sky search for short gravitational-wave bursts in the second advanced ligo and advanced virgo run. *Phys. Rev. D.* **100**, 024017 (2019).
63. Abbott, B. P. Search for the isotropic stochastic background using data from advanced ligo's second observing run. *Phys. Rev. D.* **100**, 061101 (2019).

64. Akrami, Y. Promise of future searches for cosmic topology. *Phys. Rev. Lett.* **132**, 171501 (2024).
65. Ellis, G. F. R. The Bianchi models: Then and now. *Gen. Relativ. Gravit.* **38**, 1003–1015 (2006).
66. Hersbach, H. The era5 global reanalysis. *Q. J. R. Meteorological Soc.* **146**, 1999–2049 (2020).
67. Agarwal, A. et al. Network-based identification and characterization of teleconnections on different scales. *Sci. Rep.* **9**, 8808 (2019).
68. Strnad, F. M., Schlör, J., Fröhlich, C. & Goswami, B. Teleconnection patterns of different el niño types revealed by climate network curvature. *Geophys. Res. Lett.* **49**, e2022GL098571 (2022).
69. Spengler, C. The adhesion capability of Staphylococcus aureus cells is heterogeneously distributed over the cell envelope. *Soft Matter* **20**, 484–494 (2024).
70. Praetorius, S., Voigt, A., Wittkowski, R. & Löwen, H. Active crystals on a sphere. *Phys. Rev. E* **97**, 052615 (2018).
71. Nitschke, I., Reuther, S. & Voigt, A. Hydrodynamic interactions in polar liquid crystals on evolving surfaces. *Phys. Rev. Fluids* **4**, 044002 (2019).
72. Hsu, C.-P., Sciortino, A., de la Trobe, Y. A. & Bausch, A. R. Activity-induced polar patterns of filaments gliding on a sphere. *Nat. Commun.* **13**, 2579 (2022).
73. Dlamini, N., Prestipino, S. & Pellicane, G. Self-Assembled Structures of Colloidal Dimers and Disks on a Spherical Surface. *Entropy* **23**, 585 (2021).
74. ESA & Planck Collaboration. Planck legacy archive http://pla.esac.esa.int (2024).
75. Planck Collaboration I. *Planck* 2018 results. I. Overview, and the cosmological legacy of *Planck*. *AA* **641**, A1 (2020).
76. Planck Collaboration IV. *Planck* 2018 results. IV. Diffuse component separation. *AA* **641**, A4 (2020).
77. Planck Collaboration XII. *Planck* 2015 results. XII. Full Focal Plane simulations. *AA* **594**, A12 (2016).
78. Hivon, E. et al. Healpix fortran facility user guidelines: anafast https://healpix.sourceforge.io/html/fac_anafast.htm (2024).
79. Misner, C. W., Thorne, K. S. & Wheeler, J. A. *Gravitation* (W. H. Freeman and Company, San Francisco, 1973).
80. Zonca, A. healpy: equal area pixelization and spherical harmonics transforms for data on the sphere in python. *J. Open Source Softw.* **4**, 1298 (2019).
81. Martinez-Castellanos, I. Multiresolution healpix maps for multiwavelength and multimessenger astronomy. *Astronom. J.* **163**, 259 (2022).

Acknowledgements

We thank Daniel Hug for valuable discussions on integral geometry. M.A.K. acknowledges funding and support by the Deutsche Forschungsgemeinschaft (DFG, German Research Foundation) through the SPP 2265, under grant numbers KL 3391/2-2, WI 5527/1-1 and LO 418/25-1, and by the Initiative and Networking Fund of the Helmholtz Association through the Project "DataMat". This research made use of observations obtained with Planck (http://www.esa.int/Planck), an ESA science mission with instruments and contributions directly funded by ESA Member States, NASA, and Canada. Some of the results in this paper have been derived using the healpy and HEALPix packages[50,80].

Author contributions

C.R., M.A.K., M.S., and C.C. conceived the presented idea. C.C. designed and implemented the computational framework, analyzed the data, and wrote the first draft. C.C. and M.A.K. wrote the manuscript with support from C.R. C.R. and M.A.K. supervised the project. A.J.B. supervised the Planck data analysis. All authors reviewed the manuscript.

Funding

Open Access funding enabled and organized by Projekt DEAL.

Competing interests

The authors declare no competing interests.

Additional information

Supplementary information The online version contains supplementary material available at https://doi.org/10.1038/s42005-024-01751-1.

Correspondence and requests for materials should be addressed to Caroline Collischon.

Peer review information *Communications Physics* thanks the anonymous reviewers for their contribution to the peer review of this work. A peer review file is available.